Draft version January 27, 2016
Preprint typeset using LaTeX style emulateapj v. 5/2/11

arXiv:1601.06798v1 [astro-ph.GA] 25 Jan 2016

DUAL STELLAR HALOS IN THE STANDARD ELLIPTICAL GALAXY M105 AND FORMATION OF MASSIVE EARLY-TYPE GALAXIES

Myung Gyoon Lee & In Sung Jang
Astronomy Program, Department of Physics and Astronomy, Seoul National University, 1 Gwanak-ro, Gwanak-gu, Seoul 151-742, Korea

Draft version January 27, 2016

ABSTRACT

M105 is a standard elliptical galaxy, located in the Leo I Group. We present photometry of the resolved stars in its inner region at $R \approx 4' \approx 4R_{\rm eff}$, obtained from F606W and F814W images in the *Hubble Space Telescope* archive. We combine this with photometry of the outer region at $R \approx 12' \approx 12R_{\rm eff}$ from archival imaging data. Color-magnitude diagrams of the resolved stars in the inner region show a prominent red giant branch (RGB) with a large color range, while those of the outer region show better a narrow blue RGB. The metallicity distribution function (MDF) of the RGB stars shows the existence of two distinct subpopulations: a dominant metal-rich population (with a peak at [M/H]≈ 0.0) and a much weaker metal-poor population (with a peak at [M/H]≈ -1.1). The radial number density profiles of the metal-rich and metal-poor RGB stars are fit well by a Sérsic law with $n = 2.75 \pm 0.10$ and $n = 6.89 \pm 0.94$, and by a single power law ($\sigma \propto R^{-3.8}$ and $\sigma \propto R^{-2.6}$), respectively. The MDFs of the inner and outer regions can be described well by accretion gas models of chemical evolution with two components. These provide strong evidence that there are two distinct stellar halos in this galaxy, metal-poor and red metal-rich halos, consistent with the results based on globular cluster systems in bright early-type galaxies (Park & Lee 2013). We discuss the implications of these results with regard to the formation of massive early-type galaxies in the dual halo mode formation scenario.

Subject headings: galaxies: distances and redshifts — galaxies: individual (M105) — galaxies: stellar content—galaxies:structure — galaxies:elliptical and lenticular, cD — galaxies:halo

1. INTRODUCTION

Globular clusters are an excellent probe to investigate the halos in nearby galaxies. Color distributions of globular clusters in early-type galaxies (ETGs), including elliptical and lenticular galaxies, show that there are two subpopulations: blue (metal-poor) and red (metal-rich) globular clusters (Geisler et al. 1996; Brodie & Strader 2006; Peng et al. 2008). Recently Park & Lee (2013) investigated the spatial distribution of these subpopulations in 23 Virgo ETGs using a homogeneous data set based on the ACSVCS catalog, which was derived from the observations with the Hubble Space Telescope (HST) (Jordán et al. 2009). They found that the ellipticity of the red globular cluster systems (GCSs) follows much more tightly than that of the stellar light, compared with the ellipticity of the blue GCSs. From this and other related properties of the GCSs they suggested that massive ETGs may have dual halos: a blue (metal-poor) halo and a red (metal-rich) halo. The red halos are much more elongated and centrally concentrated than the blue halos. The red halos may have stronger rotation than the blue halos. They predicted that ETGs may host stellar halos corresponding to these two halos. However, the number density of the blue halo stars in ETGs is much lower than that of the red halo stars in the outer region of their host galaxies so that it is not easy to see the blue halo stars in typical images of ETGs. Typical images of ETGs show only the structure of the red halos that dominate the integrated light.

Indeed the existence of blue (metal-poor) RGB stars in ETGs was studied for a few nearby galaxies: NGC 3115 (S0), NGC 5128 (Ep), NGC 3377 (E5), and M105 (NGC 3379, E1) (Elson 1997; Harris & Harris 2002; Rejkuba et al. 2005, 2011; Crnojević et al. 2013; Harris et al. 2007a,b; Bird et al. 2015; Peacock et al. 2015). In her pioneering study of stars in an *HST*/WFPC2 field $5'$ (22 kpc) away from the major axis of NGC 3115, an edge-on bright S0 galaxy, Elson (1997) found that the $(V-I)$ color distribution of the resolved red giants in this field shows a clear bimodality. Then she pointed out that there are two distinct halo populations of roughly equal size: a metal-poor halo with [Fe/H] ≈ -1.3 and a metal-rich one with [Fe/H] ≈ -0.0. This bimodality was confirmed later in a recent study of the resolved stars in the more remote fields of this galaxy based on deeper photometry by Peacock et al. (2015).

Resolved stars in NGC 5218 were extensively studied by Harris & Harris (2002); Rejkuba et al. (2005, 2011); Crnojević et al. (2013); Rejkuba et al. (2014) and Bird et al. (2015). Because of the presence of notable dust lane in the middle, whether the morphological type of NGC 5128 is pecular S0 or E has been controversial. In a recent review, Harris (2010) concluded that it is an Ep, noting that its global properties are closer to normal Es, except for the dust lane. NGC 5128 covers a very large angular size in the sky so that deep images were obtained only for a part of the entire galaxy. Harris et al. (2007a) studied the resolved stars in NGC 3377, a highly elongated E5 galaxy with intermediate luminosity ($M_V = -19.9$ mag), finding that the mean metallicity of these stars is between those of massive galaxies and dwarf galaxies.

mglee@astro.snu.ac.kr, isjang@astro.snu.ac.kr

TABLE 1
Basic Parameters of M105

Parameter	Value	References
R.A.(J2000), Dec(J2000)	10 47 49.6, +12 34 54	1
Morphological Type	E1	2
Total magnitude and color	$B^T = 10.24 \pm 0.03$, $(B^T - V^T) = 0.96 \pm 0.01$	2
Ellipticity	0.11	3
Position angle	71 deg	3
$D_{25}(B)$	$262''$	2
Effective radius	$58\farcs7$	2
Systemic velocity	911 km s^{-1}	1
Central velocity dispersion ($R_{\rm eff}/8$)	213 km s^{-1}	4
Foreground reddening	$E(B-V) = 0.022$	5
Distance	$(m-M)_0 = 30.05 \pm 0.02$(ran) ± 0.12(sys)	6
Plate scale	49.6 pc arcsec^{-1}	6
Absolute total magnitudes	$M_B^T = -19.89$, $M_V^T = -20.83$	6

References. — (1) NED; (2) de Vaucouleurs (1991); (3) Makarov et al. (2014); (4) Cappellari et al. (2013); (5) Schlafly & Finkbeiner (2011); (6) This study.

In this study we investigate the resolved stars in M105, a nearby E1 galaxy in the Leo I Group that is located at 10.6 Mpc (Lee & Jang 2013). M105 is located at the distance that is ideal for studying not only its resolved stars but also their radial distribution, if we use high resolution images. M105 has been known as one of the standard elliptical galaxies of which the surface brightness profile can be described impressively over many orders of magnitudes by the de Vaucouleurs $R^{1/4}$ law (de Vaucouleurs & Capaccioli 1979; Capaccioli et al. 1990; Watkins et al. 2014). Basic parameters of M105 are listed in **Table 1**. Foreground reddening toward M105 is known to be very small, $E(B-V) = 0.022$ (Schlafly & Finkbeiner 2011). Corresponding values are $A_I = 0.037$ and $E(V-I) = 0.030$. Internal reddening for the old red giants in elliptical galaxies must be low so that it is assumed to be zero in this study.

Resolved stars in M105 were studied previously by Sakai et al. (1997); Gregg et al. (2004) and Harris et al. (2007b). Sakai et al. (1997) estimated the distance to this galaxy using the tip of the red giant branch (TRGB) method (Lee et al. 1993), from the photometry of the resolved stars in the *HST*/WFPC2 F814W images of a field $6'$ west of M105 . However, they had only one-band images so that they had no color information of the resolved stars. Gregg et al. (2004) presented F110W(J) and F160W(H) photometry of the resolved stars in three small fields at $R = 3'$, $R = 4\farcm5$, and $R = 6'$, based on *HST* NICMOS images. They found that the resolved stars have a broad range of metallicity from [Fe/H]~ -1.5 to $+0.8$, with a mean of the solar metallicity. They pointed out that the stellar population in their fields is similar to that of the bulge of the Milky Way Galaxy. Harris et al. (2007b) observed a remote western field at $R = 12'$ ($\approx 12R_{\rm eff}$), using *HST*/ACS F606W and F814W filters. They carried out a better TRGB determination than the previous literature, being able to work with two color photometry. They found that the metallicity distribution function (MDF) of the red giant stars in this field is very broad and flat, showing no dominant population. They stated that the shape of this MDF is not like any known MDFs of other galaxies. They suggested also that the resolved stars in this remote region is composed of two distinct subpopulations, metal-poor and metal-rich populations, noting that the metal-poor stars get more significant than the metal-rich stars with increasing radius in this outer region.

In this study we present photometry of the resolved stars in the inner region ($2' < R \leq 6'$) of M105, obtained from F606W and F814W images in the *HST* archive. Then we combine this with the photometry of the outer region studied previously by Harris et al. (2007b), to investigate the stellar populations over a large radial range. Section 2 derives photometry of the point sources in the images and §3 presents color-magnitude diagrams (CMDs) of the resolved stars in this galaxy, derives a distance to this galaxy using the TRGB method, estimates metallicities of bright RGB stars, presents their MDFs, and shows the radial distributions of the metal-poor and metal-rich RGB stars. In §4 we investigate the MDFs of the RGB stars in M105 with analytic chemical evolution models, compare the MDFs of M105 with those of other nearby galaxies, and suggest an updated dual halo mode scenario for the formation of massive ETGs. Primary results are summarized in the final section.

2. DATA REDUCTION AND ANALYSIS

2.1. *Data Reduction*

There are three bright galaxies around the center of the Leo I Group: M105, NGC 3384 (SB0), and NGC 3389 (Sc(s)). NGC 3389 is known to be located about 10 Mpc behind M105 and NGC 3384 both of which are at similar distances (Stierwalt et al. 2009; Bose & Kumar 2014). NGC 3389 belongs to another small group in the Leo I Cloud that is behind the Leo I Group (Stierwalt et al. 2009). **Figure 1** displays a finding chart for M105, showing the *HST* fields on the SDSS color image. F606W and F814W images of two fields in M105 are available in the *HST* archive, as marked in this figure and listed in **Table 2** : a south-eastern inner field (called the M105–SE field), and a western outer field (called the M105–W field) that was used previously for the study of resolved stars by Harris et al. (2007b). The M105–SE field is located at $R \sim 4'$ from the galaxy center, while the M105–W field is at $R \sim 12'$.

We combined the images of the M105–SE and W

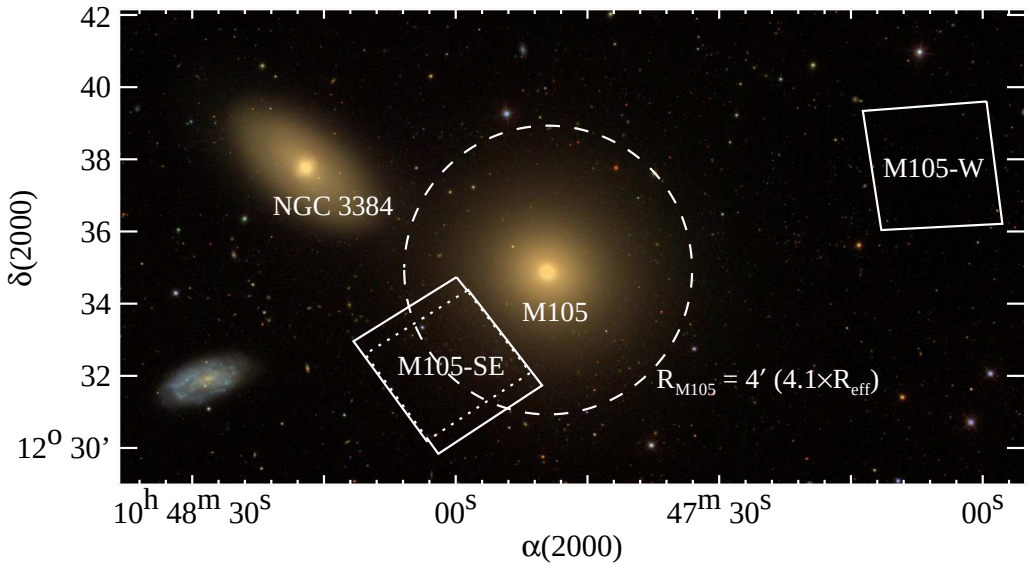

FIG. 1.— A finding chart for M105 (E1). HST fields used in this study are marked on the color map of the Sloan Digital Sky Survey: one inner field M105-SE (at $R \approx 4R_{\rm eff} \approx 12$ kpc) and one outer field M105-W (at $R \approx 12R_{\rm eff} \approx 36$ kpc). The dashed-line represents a circle with $4'$ radius centered on M105. NGC 3384 (SB0) is also marked in the north east of M105. A spiral galaxy in the south-east region, NGC 3389 (Sc(s)), is known to be a background galaxy, being located about 10 Mpc behind M105.

TABLE 2
A SUMMARY OF *HST* DATA FOR M105

Field	R.A. (2000)	Dec (2000)	Instrument	Exposure time [sec] F606W	F814W	Prop. ID
M105-SE	10 48 01.53	12 32 28.2	ACS/WFC	9,775	9,775	10413
	10 48 00.20	12 32 06.8	ACS/WFC	9,775	9,775	10413
M105-W	10 47 05.67	12 37 49.8	ACS/WFC	38,500	22,260	9811

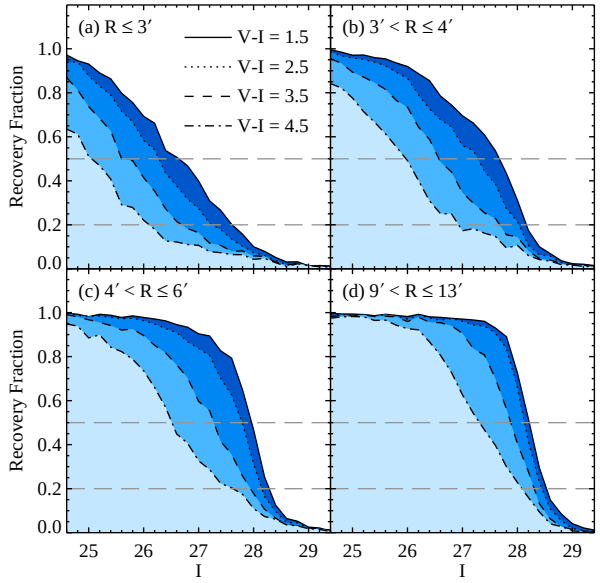

FIG. 2.— Recovery fractions of artificial stars as a function of I-band magnitude: (a) $R \leq 3'$, (b) $3' < R \leq 4'$, (c) $4' < R \leq 6'$, and (d) $9' < R \leq 13'$. Curved lines indicate the recovery rates (completeness) of artificial stars with different $V-I$ color (solid lines for $V-I = 1.5$ stars, dotted lines for $V-I = 2.5$ stars, short dashed lines for $V-I = 3.5$ stars, and dot-dashed lines for $V-I = 4.5$ stars, respectively). Upper and lower horizontal dashed lines in each panel represent 50% and 20% recovery rates, respectively.

fields to make a mosaic drizzled image for the entire observed field, using Tweakreg and AstroDrizzle tasks in DrizzlePac provided by the Space Telescope Science Institute (STScI) (http://www.stsci.edu/hst/HST_overview/drizzlepac/), as done in Jang & Lee (2014). The final images have a pixel scale, $0''.03$ per pixel. Total exposure times are 19,550 s for each of F606W and F814W. These exposure times are slightly shorter than those for the M105-W field, but are still long enough to study the resolved stars in the M105-SE field.

2.2. *Photometry and Completeness Test*

We derived photometry of the point sources in the drizzled images using IRAF/DAOPHOT package (Stetson 1994), as done in Jang & Lee (2014). We selected the point sources using the sharpness parameters provided by DAOPHOT. Then we converted the instrumental magnitudes of the sources to the standard Johnson-Cousins VI Vega magnitudes, following Sirianni et al. (2005).

We estimated the completeness of our photometry using artificial star experiments. First, we selected four $0.5' \times 0.5'$ subregions at different galactocentric radii. We generated artificial stars with colors $(V-I) = 0.1 - 4.9$ (in steps of 0.2 mag) and magnitudes $I = 24.5 - 30.0$ mag. Then we added ∼5000 (about 10 % of the detected point sources) artificial stars in each sub-region, and iterated this procedure four times to increase the total number

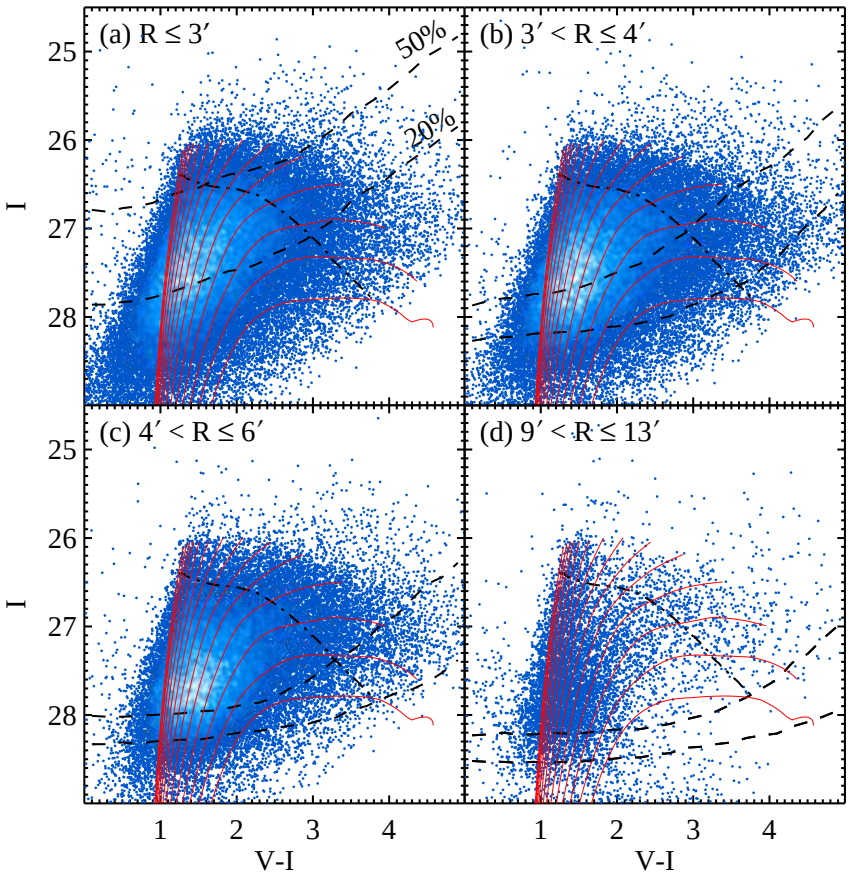

FIG. 3.— $I-(V-I)$ CMDs of the resolved stars in M105: (a) $R \leq 3'$, (b) $3' < R \leq 4'$, (c) $4' < R \leq 6'$, and (d) $9' < R \leq 13'$. Smoothed maps display the number density maps for the high density regions (Hess diagrams). Red solid lines represent theoretical isochrones for 12 Gyr age, [α/Fe]=0.2, and a range of metallicity ([Fe/H] = –2.4 to +0.2 ([M/H] = –2.2 to +0.4) with a step of 0.2 from left to right) in the Dartmouth models (Dotter et al. 2008). Upper and lower dashed lines in each panel represent 50% and 20% completeness limits, respectively.

of artificial stars. We estimated the recovery rate (completeness) from the ratio of the number of the recovered stars and that of the added stars. **Figure 2** presents the completeness as a function of I magnitudes for four color values ($(V-I) = 1.5, 2.5, 3.5$, and 4.5). The 50% completeness levels for $(V-I) = 3.5$ are $I \approx 28.0$ mag at the outer region, and they get brighter as the color gets redder or the galactocentric distance decreases.

3. RESULTS

3.1. *CMDs of the Resolved Stars*

In **Figure 3** we display CMDs of the resolved stars in the four ranges of projected galactocentric distance of M105: (a) $2' < R \leq 3'$, (b) $3' < R \leq 4'$, (c) $4' < R \leq 6'$, and (d) $9' < R \leq 13'$. The M105-SE field covers $2' \lesssim R \lesssim 6'$, while the M105-W field covers $9' \lesssim R \lesssim 13'$. We plotted a Hess diagram for the region with high number density in the CMDs to show better the details. The dashed lines denote 50% and 20% completeness, and the dot-dashed line represents $M_{\rm bol} = -3.0$ mag. For reference we overlayed theoretical RGB loci of the 12 Gyr isochrones for [α/Fe] = 0.2 and a range of metallicity ([Fe/H] = –2.4 to 0.2 with a step of 0.2 from left to right) in the Dartmouth models (Dotter et al. 2008). They were shifted according to the distance and foreground reddening of M105. We adopted [M/H] = [Fe/H]+[α/Fe], where [α/Fe] = 0.2.

A few distinguishable features are noted in **Figure 3**. First, most of the resolved stars in M105 are RGB stars. The RGB stars show a large range of color, indicating that their metallicity ranges from very low ([Fe/H]≈ -2.4) to solar metallicity or higher. The sources brighter than the RGB stars appear to be a combination of old asymptotic giant branch (AGB) stars, foreground stars, and blended stars due to crowding, as discussed in the study of the M105-W field by Harris et al. (2007b). Second, the RGB in the outer region ($9' < R \leq 13'$) in **Figure 3(d)** shows clearly two distinguishable components: a narrow blue RGB and a wider red RGB, as shown also by Harris et al. (2007b). The blue RGB is more clearly seen in this outer region than in the inner regions. It is noted that our photometry of the outer region goes about one magnitude deeper for the red stars than that of the same region given by Harris et al. (2007b), although both studies used the same raw data. The 50% completeness limit for $(V-I) = 3.0$ is $I \approx 28.0$ mag in our photometry, while it is $I \approx 26.8$ mag in Harris et al. (2007b) (their **Figure 3**). We infer that this difference is mainly due to the improvement of image combining in the drizzle package used in this study. Third, the positions of the isochrones for 12 Gyrs are consistent with the RGB in the CMDs, indicating that the RGB stars are mostly very old.

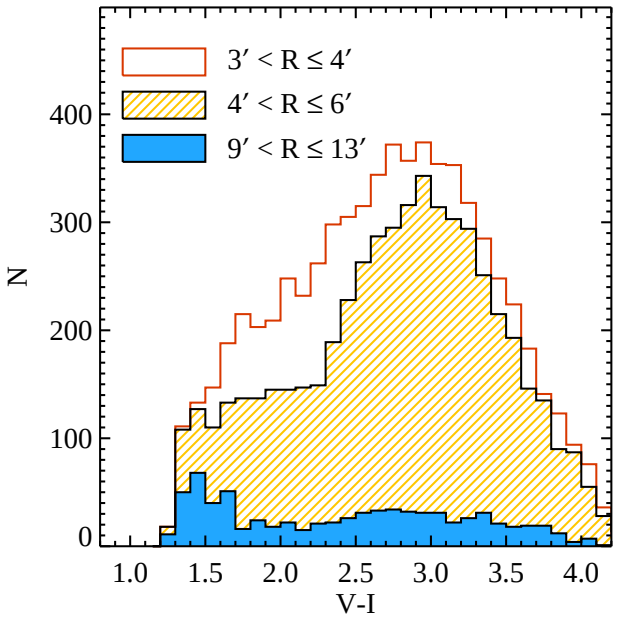

FIG. 4.— $(V-I)$ color distributions of the bright RGB stars $(-3.7 < M_{\rm bol} \leq -3.0)$ at $3' < R \leq 4'$ (open histogram), $4' < R \leq 6'$ (hatched histogram), and $9' < R \leq 13'$ (filled histogram).

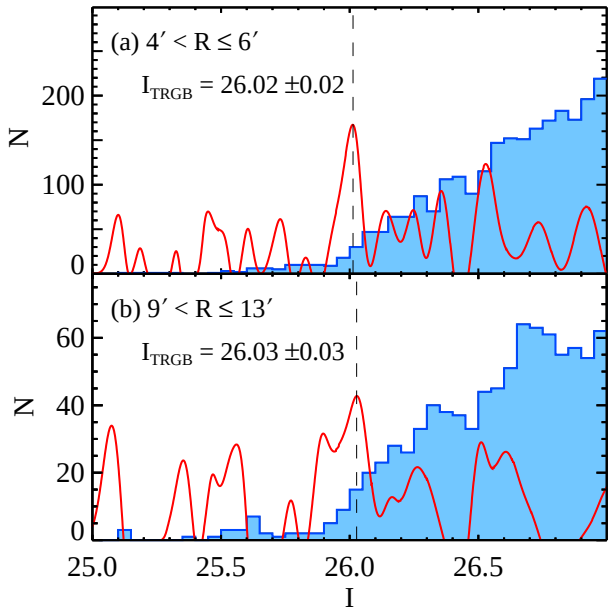

FIG. 5.— I-band luminosity functions (histograms) and its corresponding edge detection response functions (red solid lines) for the red giants with $1.2 < (V-I) \leq 2.0$ at $4' < R < 6'$ (a) and $9' < R < 13'$ (b).

In **Figure 4** we plotted the $(V-I)$ color distribution of the bright RGB stars $(-3.7 < M_{\rm bol} \leq -3.0)$ in the inner $(3' < R \leq 4'$ and $4' < R \leq 6')$ and outer $(9' < R \leq 13')$ regions. We derived $M_{\rm bol}$ of the RGB stars as described in the next section. The color distributions of the bright RGB stars in the outer region of M105 show a clear bimodality: a narrow blue component with a color range of $1.2 < (V-I) < 1.7$ and a peak at $(V-I) \approx 1.5$, and a broad red component with a color range of $1.8 < (V-I) < 4.1$ and a peak at $(V-I) \approx 2.8$. The blue peak is higher than the red peak in this outer region. The color distribution of the bright RGB stars in the inner region of M105 shows also a bimodality, but in a weaker contrast than that of the outer region.

3.2. *Distance Estimation*

We determined a distance to M105 using the TRGB method (Lee et al. 1993; Sakai et al. 1996; Rizzi et al. 2007) as follows. First, we derived the I-band luminosity functions of the red giants in the inner and outer regions $(4' < R \leq 6'$ and $9' < R \leq 13')$ of M105 where crowding is not so severe. The RGB stars show a broad range of color. We selected relatively blue stars with $1.2 < (V-I) < 2.0$ among the RGB stars for better measurement of the TRGB, and derived their I-band luminosity functions as shown in **Figure 5**.

Using the edge-detecting algorithm (Méndez et al. 2002; Sakai et al. 1996) weighted according to the number of stars in each magnitude bin, we determined the TRGB magnitude more quantitatively. From the luminosity function $\Phi(m)$, we calculated an edge-detection response function $E(m)$ $(= \sqrt{\Phi}[\log(\Phi(m+\sigma_m)) - \log(\Phi(m-\sigma_m))])$, where σ_m is the mean photometric error within a bin of ± 0.05 mag about magnitude m. They were plotted by the solid lines in **Figure 5**. The errors for the TRGB magnitudes were obtained using the bootstrap resampling method. In each simulation we resampled randomly the RGB sample with replacement to make a new sample of the same size. We performed one thousand simulations. We estimated the TRGB magnitude for each simulation using the same procedure, and derived the standard deviation of the estimated TRGB magnitudes.

Thus estimated TRGB magnitude for the inner region is $I_{\rm TRGB} = 26.02 \pm 0.02$, which is almost the same as that for the outer region, $I_{\rm TRGB} = 26.03 \pm 0.03$. The median color of the TRGB is derived from the colors of the selected bright red giants close to the TRGB: $(V-I)_{\rm TRGB} = 1.61 \pm 0.02$ for the inner region, and 1.54 ± 0.03 for the outer region. We used the TRGB calibration given in Rizzi et al. (2007): $M_{\rm I,TRGB} = -4.05(\pm 0.02) + 0.217(\pm 0.01)((V-I)_0 - 1.6)$ (where $(V-I)_0$ is a reddening corrected color of the TRGB) with a systematic error of 0.12. After correction for foreground reddening, we derived a distance modulus $(m-M)_0 = 30.04 \pm 0.02$ for the inner region, and 30.07 ± 0.03 for the outer region. We adopted a mean of these two estimates, $(m-M)_0 = 30.05 \pm 0.02$ with a systematic error of 0.12 (corresponding to a linear distance of 10.23 ± 0.09 Mpc). At this distance one arcsec corresponds to 49.6 pc. The results of distance estimation for M105 are summarized in **Table 3**. This shows that M105 is located at the distance similar to those of M66, M96, and NGC 3377 in the same Leo I Group (Lee & Jang 2013).

The distance to M105 was estimated using various methods in the past. Our estimate based on the TRGB method ($(m-M)_0 = 30.05 \pm 0.02({\rm ran}) \pm 0.12({\rm sys})$) is consistent with those derived using the planetary nebula luminosity function (30.09 ± 0.09 (Ciardullo et al. 1993), 29.98 ± 0.11 (Ciardullo et al. 2002)), and the surface brightness fluctuation method (30.32 ± 0.14 (Tonry et al. 2001), and 30.16 ± 0.14 (Jensen et al. 2003)). However, our value is much smaller than those based on the globular cluster luminosity function. Larsen et al. (2001) de-

TABLE 3
A Summary of TRGB Distance Measurements for M105

Parameter	M105-SE	M105-W
TRGB magnitude, I_{TRGB}	26.02 ± 0.02	26.03 ± 0.03
TRGB color, $(V-I)_{TRGB}$	1.61 ± 0.02	1.54 ± 0.03
Foreground extinction at V, A_V	0.071	0.062
Foreground extinction at I, A_I	0.039	0.034
Foreground reddening, $E(V-I)$	0.032	0.028
Intrinsic TRGB magnitude $I_{0,TRGB}$	25.98 ± 0.03	26.00 ± 0.03
Intrinsic TRGB color, $(V-I)_{0,TRGB}$	1.58 ± 0.03	1.51 ± 0.03
Absolute TRGB magnitude, $M_{I,TRGB}$	-4.06	-4.07
Distance modulus, $(m-M)_0$	30.04 ± 0.02	30.07 ± 0.03
	mean $= 30.05 \pm 0.02 \pm 0.12$	
Distance	10.17 ± 0.09 Mpc	10.30 ± 0.14 Mpc
	mean $= 10.23 \pm 0.08$ Mpc	

rived 30.93 ± 0.12 from the total globular cluster sample, 31.92 ± 0.30 from the red globular cluster sample, and 30.15 ± 0.12 from the blue globular cluster sample. The first two values are much larger than ours, while the last is consistent with ours. However, these estimates were based on a small number of globular clusters (30 blue globular clusters and 24 red globular clusters with $20 < V < 24$ mag) so that their estimates must suffer from a significant uncertainty.

There are a few studies of the TRGB distance measurements for M105 in the literature. Sakai et al. (1997) presented TRGB measurements, $I_{TRGB} = 26.32 \pm 0.05$ and $(m-M)_0 = 30.30 \pm 0.14$ (adopting $A_I = 0.05$), from the *HST*/WFPC2 images. Their TRGB magnitude is 0.3 mag fainter than our measurement, $I_{\rm TRGB} = 26.03 \pm 0.03$. It is noted that Sakai et al. (1997) used only F814W images for their analysis, while we used much deeper F606W and F814W images. Gregg et al. (2004) also derived a distance estimate from the F160W band TRGB magnitude based on the HST/NICMOS images, $(m-M)_0 = 30.14 \pm 0.14$. Later Harris et al. (2007b) presented TRGB measurements based on the same HST/ACS images of the M105-W field as used in this study, $I_{TRGB} = 26.10 \pm 0.10$ and $(m-M)_0 = 30.06 \pm 0.10$. Thus the values for the TRGB magnitude and distance in this study, Harris et al. (2007b), and Gregg et al. (2004) are in excellent agreement, but these TRGB values are 0.2 to 0.3 mag brighter than the value given by Sakai et al. (1997).

3.3. *MDFs of the RGB Stars*

We estimate the metallicity ([M/H]) of the bright RGB stars in M105, comparing their $(V-I)$ colors with the theoretical isochrones, following the method used in Harris et al. (2007a,b). We assumed that the mean age of the stars in this galaxy is 12 Gyr, as found from spectroscopic measurement of mean ages of the stellar populations in the regions at 2.6–3.5 $R/R_{\rm eff}$ of M105 by Weijmans et al. (2009).

In **Figure 6** we plotted the CMDs for the RGBs of 12 Gyr isochrones in the Dartmouth models (Dotter et al. 2008) in comparison with one of the recent models for old stellar populations, the Victoria-Regina models (VandenBerg et al. 2012, 2014). We also overlayed the RGB sequences of five Milky Way globular clusters (Da Costa & Armandroff 1990): M15 ([Fe/H] $= -2.37$), M2 ([Fe/H] $= -1.65$), NGC 1851 ([Fe/H] $= -1.18$), 47 Tuc (NGC 104, [Fe/H] $= -0.72$), NGC 6553 ([Fe/H] $= -0.18$), and one old open cluster NGC 6791 ([Fe/H] $= +0.2$ to $+0.35$) (Garnavich et al. 1994; Chaboyer et al. 1999). The [Fe/H] values of the globular clusters are from the 2010 edition of the catalog of the Milky Way globular clusters (Harris 1996). NGC 6791 is known to be 8.5 Gyr old, a few Gyrs younger than the globular clusters, and its metallicity is estimated to be [Fe/H]= +0.20 to +0.35 (Harris & Harris 2000; VandenBerg et al. 2014).

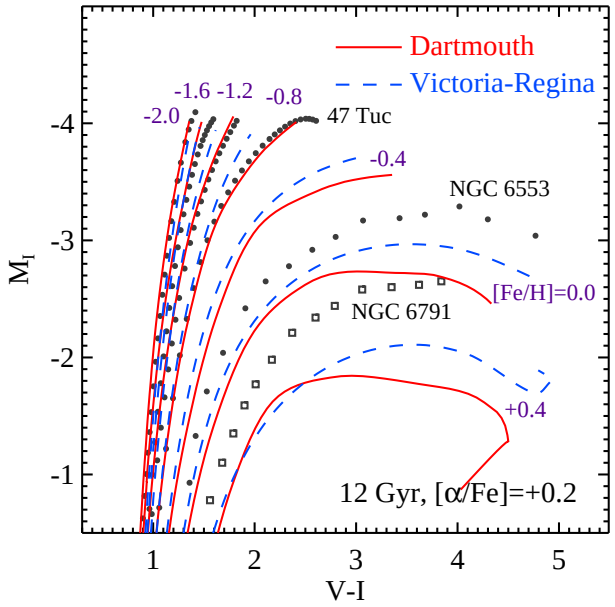

Fig. 6.— RGBs of 12 Gyr isochrones for [α/Fe]=+0.2 and [Fe/H]=–2.0, –1.6, –1.2, –0.8, –0.4, 0.0, and +0.4 in the Dartmouth models (Dotter et al. 2008) (solid lines) and in the Victoria-Regina models (VandenBerg et al. 2014) (dashed lines). Dotted lines represent the RGB sequences of five galactic globular clusters (Da Costa & Armandroff 1990; Harris 1996): M15 ([Fe/H]= −2.37), M2 ([Fe/H]= −1.65), NGC 1851 ([Fe/H]= −1.18), 47 Tuc (NGC 104) (Fe/H]= −0.72), and NGC 6553 ([Fe/H]= −0.18), Open squares denote the RGB sequence of NGC 6791, an old open cluster with [Fe/H]= +0.3 and age of 8.5 Gyr (Garnavich et al. 1994; Chaboyer et al. 1999; VandenBerg et al. 2014).

A comparison of the Dartmouth isochrones with the RGBs of the globular clusters shows that the isochrones for [Fe/H] = –2.0, –1.6, –1.2, and –0.8 are roughly in agreement with the RGBs of M15, M2, NGC 1851, and 47 Tuc, respectively. The RGB of the metal-rich bulge globular cluster NGC 6553 with [Fe/H] $= -0.18$ is seen

between the Dartmouth isochrones for [Fe/H] = –0.4 and [Fe/H] = 0.0, and that of the old open cluster NGC 6791 is located between the isochrones for [Fe/H] = 0.0 and [Fe/H] = +0.4. On the other hand, the Victoria-Regina isochrones are slightly redder for [Fe/H] = –2.0, similar for [Fe/H] = –1.6, and bluer or brighter than for [Fe/H] > −1.6, compared with the Dartmouth isochrones.

The RGBs of the isochrones become redder (cooler) as the value of [α/Fe] increases. We adopted, as a reference value, [α/Fe] = +0.2, for the study of the resolved stars with a large range of metallicity in M105. In this study we used the Dartmouth isochrones as provided. It is noted that recognizing the difference between the old versions of Victoria-Regina models and the RGB sequences of clusters, Harris & Harris (2000, 2002) adjusted slightly the colors of the isochrones using the cluster sequence for their study of the MDFs.

We derived a metallicity of each star in M105 from the comparison of the CMDs with the Dartmouth isochrones. The problem due to the curvature of the RGBs for high metallicity is more serious in the (M_I, $(V-I)_0$) plane compared with in the ($M_{\rm bol}$, $(V-I)_0$) plane so some of the previous studies adopted the latter plane for interpolation (Harris & Harris 2000, 2002). However, it is not easy to convert an observational (M_I, $(V-I)_0$) plane of stars to an ($M_{\rm bol}$, $(V-I)_0$) plane for the metal-rich stars because of the significantly curved RGB sequences, while it is straightforward to convert a theoretical ($M_{\rm bol}$, $(V-I)_0$) plane of models to an (M_I, $(V-I)_0$) plane. Therefore we used (M_I, $(V-I)_0$) planes rather than ($M_{\rm bol}$, $(V-I)_0$) planes for interpolation to derive a metallicity value of each star. To reduce the uncertainties due to the curved tracks and non-linearity in the [M/H]-color relations as much as possible, we generated fine grids with steps d[M/H] = 0.01 (for [M/H]> −0.4), 0.02 (for −0.6 <[M/H]≤ −0.4), and 0.1 (for −2.4 <[M/H]≤ −0.6) using the Dartmouth models. For this we used non-linear interpolation between the tracks. Thus the errors in interpolations are supposed to be negligible.

The color range for the same metallicity range becomes wider, as the RGB stars become brighter, as seen in **Figure 3**. In addition, the photometric errors become smaller and the photometric completeness gets higher, as the stars become brighter. Therefore the derived MDFs are considered to be more reliable for brighter RGB stars. The I-band magnitudes of the reddest (the highest metallicity) stars become fainter as the color increases so that some of them may be missed, being affected by the incompleteness of our photometry. Therefore we derived the metallicity of the stars in the $M_I-(V-I)_0$ diagram where $(V-I)_0$ represents colors corrected for foreground reddening.

In **Figure 7** we display the MDFs for the bright RGB stars (with the bolometric magnitude $M_{\rm bol} \leq -3.0$ mag) in the inner region ($4' < R \leq 6'$) and the outer region ($9' < R \leq 13'$) of M105 where the completeness of our photometry is the highest. For deriving the MDFs we used the regions where photometric completeness is higher than 50% for $M_{\rm bol} = -3.0$ and [M/H]< 0.2, selecting a less crowded region at $R > 4'$ in the case of the inner field. We corrected the incompleteness of the MDFs using the completeness test results derived in this study. Completeness correction is negligible in the outer region, while it is significant in the high end of the MDFs in the inner region. However, it is noted that the peak position of the metal-rich component increased only by about 0.1 dex after completeness correction even in the inner region.

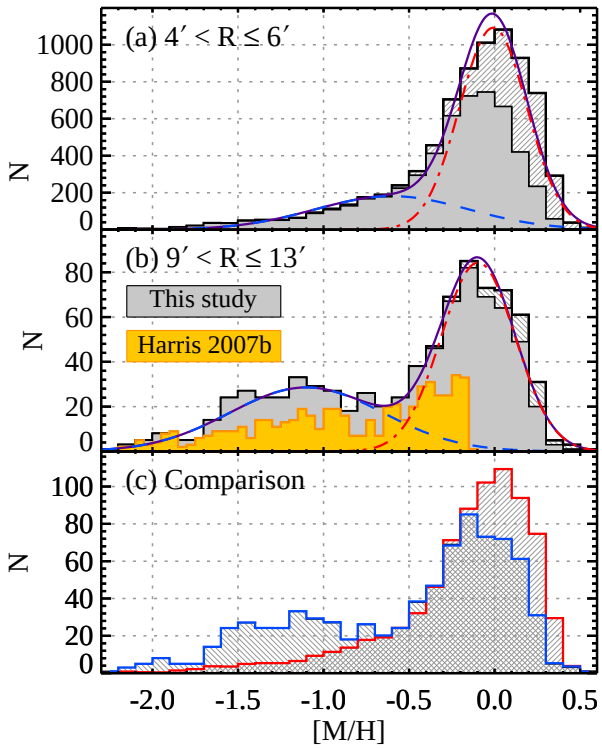

FIG. 7.— (a,b) MDFs for the bright RGB stars ($-3.7 < M_{\rm bol} \leq -3.0$) in the inner region ($4' < R \leq 6'$) and the outer region ($9' < R \leq 13'$) of M105. Filled histograms and hatched histograms show the MDFs before and after completeness correction, respectively. Blue dashed lines, red dot-dashed lines, and purple solid lines represent the double Gaussian fits for completeness-corrected MDFs: metal-poor component, metal-rich component, and their sum. The yellow histogram represents the completeness-corrected MDF of the bright RGB stars ($-3.5 < M_{\rm bol} < -3.0$) in the outer region given by Harris et al. (2007b)(their **Figure 6**). Note that their bin size is half of ours so that their numbers in each bin are about half of ours. (c) A comparison of the MDFs of the inner region (red histogram) and the outer region (blue histogram). The MDF of the inner region is scaled to match that of the outer region at [M/H] = −0.55. Note the excess of low metallicity stars in the outer region above the MDF of the inner region.

Figure 7 shows two important features as follows. First, the MDF of the outer region is clearly bimodal, showing two distinguishable components, while the visibility of the metal-poor component is much weaker in the inner region. To show this better, we scaled the MDF of the inner region to match that of the outer region at [M/H] = –0.55, and overlayed the scaled result in **Figure 7(c)**. It is seen clearly that there is a significant excess above the MDF of the inner region in the low metallicity range at [M/H] < −0.7. This is distinct from typical forms of the MDFs of stars in massive galaxies that show a single major metal-rich component with a long weak tail in the low metallicity (Harris & Harris 2002). This is also in strong contrast against the MDF of the same region given by Harris et al. (2007b) (their **Figure 6**), which is overlayed by the yellow histogram in **Figure 7(b)**. Harris et al. (2007b) pointed out that the MDF of the outer region in M105 is the broadest and flattest

TABLE 4
A Summary of Gaussian Fits for MDFs of Bright RGB stars in M105

Region	Metal-poor component			Metal-rich component		
	Center	Width	$N_{\rm total}$	Center	Width	$N_{\rm total}$
$4' < R \leq 6'$	-0.60 ± 0.04	0.45 ± 0.03	2040 ± 218	-0.01 ± 0.01	0.20 ± 0.01	5405 ± 220
$9' < R \leq 13'$	-1.10 ± 0.05	0.45 ± 0.05	320 ± 29	-0.10 ± 0.02	0.21 ± 0.01	457 ± 31

among the known MDFs of galaxies, and that they could not find any dominant subpopulation in their MDF.

To check and quantify the bimodality, we fit the data with two Gaussian functions using mpfitexpr task in IDL, as summarized in **Table 4**. We tested also the bimodality of the MDFs of these stars using the Gaussian Mixture Modelling (GMM) package program provided by Muratov & Gnedin (2010). These tests show that a unimodal distribution is rejected for both the inner and outer regions (the probability for the unimodal distribution p is much smaller than 0.1%). The MDF for the outer region is clearly bimodal with peaks at [M/H] $= -0.09$ and –1.12 (the value of the bimodality parameter, $D = 2.93 \pm 0.24$, is larger than the bimodality criterion 2), while that for the inner region is marginally bimodal with peaks at [M/H] $= -0.01$ and –0.68 (the value of D, 1.78 ± 0.03, slightly smaller but close to 2). The MDFs are reasonably well fit by the double Gaussian functions not only for the outer region but also for the inner region. However, this Gaussian function fitting is only for showing the presence of bimodality in the MDFs, without any physical justification. We will discuss these MDFs further in terms of chemical evolution models in Section 4.1.

Second, the peak metallicity of the metal-rich component in the inner region is [M/H] $= -0.01 \pm 0.01$, which is slightly higher than that for the outer region, [M/H] $= -0.10 \pm 0.02$. In contrast, the peak metallicity of the metal-poor component in the inner region is [M/H] $= -0.60 \pm 0.04$, somewhat higher than that for the outer region, [M/H] $= -1.10 \pm 0.05$. However, typical MDFs of stars in the inner regions of massive galaxies are not Gaussian, but follow a dominant quasi-gaussian form with a long tail toward the low metallicity end. Therefore the value for the genuine peak of the metal-poor component in the inner region must be much lower than [M/H] $= -0.6$, which will be shown in Section 4.1.

3.4. *Radial Distributions of the RGB Stars*

Since the MDFs of the RGB stars are bimodal, we divided the sample of bright RGB stars into two groups according to their metallicity: a metal-poor group ([M/H] ≤ -0.7), and a metal-rich group ([M/H] > -0.7). We selected a cut with [M/H] $= -0.7$, for which the MDF shows the minimum value between the two peaks in M105. Then we derived radial number density profiles of the bright stars ($I \leq 27.0$ mag) in these groups, and plotted them in **Figure 8(a)**. We corrected these profiles using the completeness data we derived in Section 2.2. We also plotted the V-band surface brightness profile (solid lines) of M105 given by Watkins et al. (2014) (in their **Figure 6**) for comparison. This surface brightness profile extends out to the semi-major axis radius, SMA$\approx 850''$, covering a wider area than the old data given in Capaccioli et al. (1990). We fit the radial number density profiles with a Sersic law (Sérsic 1963) and a power law, adopting no weighting.

Several distinguishable features are noted in this figure as follows. First, the radial number density profile of the metal-rich stars is described by a Sersic law with $n = 2.75 \pm 0.10$ for the entire range of the galactocentric radius ($3' < R < 13'$), while that of the metal-poor stars is fit well by a Sersic law with $n = 6.89 \pm 0.94$. The radial number density profile of the total sample is fit well with a Sersic index $n = 3.71 \pm 0.21$, close to the value of the de Vaucouleurs law. Second, the slopes of the radial number density profiles of both groups and the surface brightness profile are similar in the inner region. However, the slope of the radial number density profiles of the total sample is much steeper than that of the surface brightness profile in the outer region where the surface brightness is too faint to be measured reliably (Watkins et al. 2014). Third, the radial number density profile of the metal-poor stars is much flatter than that of the metal-rich stars in the outer region. Thus the radial number density profile of the metal-poor stars is more extended than that of the metal-rich stars in the outer region. Fourth, the mean number density of the metal-rich stars is much larger (several times) than that of the metal-poor stars in the inner region. The number density of the metal-poor stars become similar to that of the metal-rich stars in the outer region at $R \approx 10'$, and exceed the latter beyond $R \approx 10'$. Fifth, The effective radius for the total sample is derived to be $R_{\rm eff} = 0'.92 \pm 0'.10$, which is consistent with the effective radius of the integrated stellar light of the galaxy, $58''.7$.

Harris et al. (2007b) found that the radial profile of the metal-rich ([M/H]> -0.7) stars in the M105-W Field is fit well with a power law, $\sigma \sim R^{-6.0 \pm 0.6}$, much steeper than that of the metal-poor ([M/H]< -0.7) stars, $\sigma \sim R^{-1.2 \pm 0.7}$. We plotted these power laws by the dashed lines in **Figure 9(a)**. The radial density profiles of the outer region derived in this study are consistent with these two power laws. However, those of the inner region show large deviations from these two power laws: the radial profile of the metal-rich stars is flatter than, and that of the metal-poor stars is steeper than the values extrapolated from the Harris et al. (2007a)'s fits. The radial profiles of the metal-rich stars and metal-poor stars in the entire range are fit well by power laws with $\sigma \sim R^{-3.83 \pm 0.03}$ and $\sigma \sim R^{-2.58 \pm 0.03}$, respectively.

After subtracting the metal-rich component derived from the accreting gas model of chemical evolution in Section 4.1, the residual MDFs of the metal-poor components in the inner region and the outer region are found to be similar, as shown in **Figure 10(c)**. A cut with [M/H]< -0.7 covers 93% of the metal-poor component in the inner region, and a similar fraction, 95%, in the

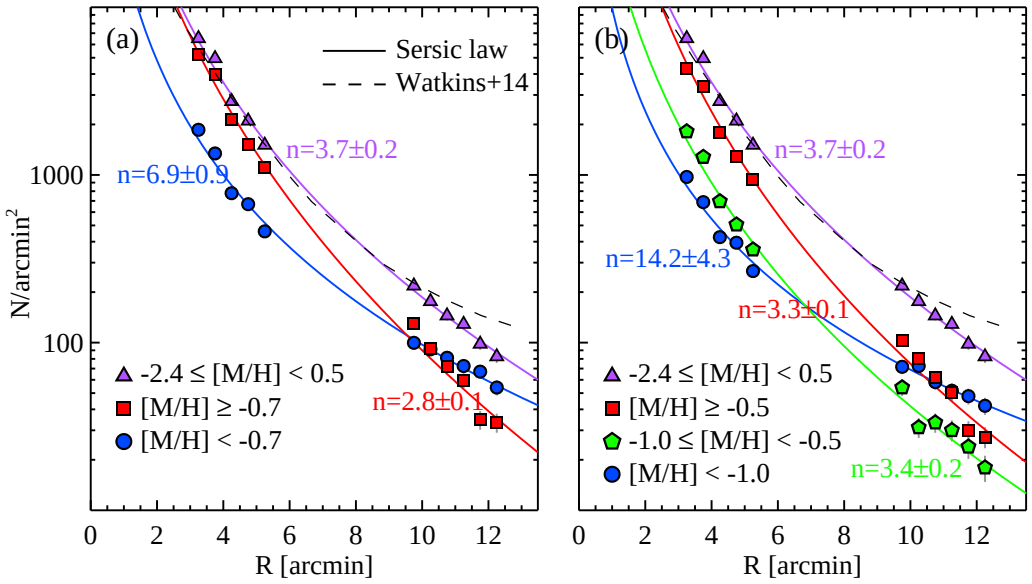

FIG. 8.— Radial number density profiles of the bright RGB stars ($I \leq 27.0$) in M105 corrected for completeness. (Left panel) Circles, squares, and triangles represent the metal-poor stars ([M/H] ≤ -0.7), metal-rich stars ([M/H] > -0.7), and all stars, respectively. (Right panel) Circles, pentagons, squares, and triangles represent the metal-poor stars ([M/H] ≤ -1.0), intermediate metallicity stars ($-1.0 <$ [M/H] ≤ -0.5), metal-rich stars ([M/H] > -0.5), and all stars, respectively. The dashed line represents the V band surface brightness profile along the major axis in Watkins et al. (2014). Solid lines represent Sersic profile fits of each stellar number density profile.

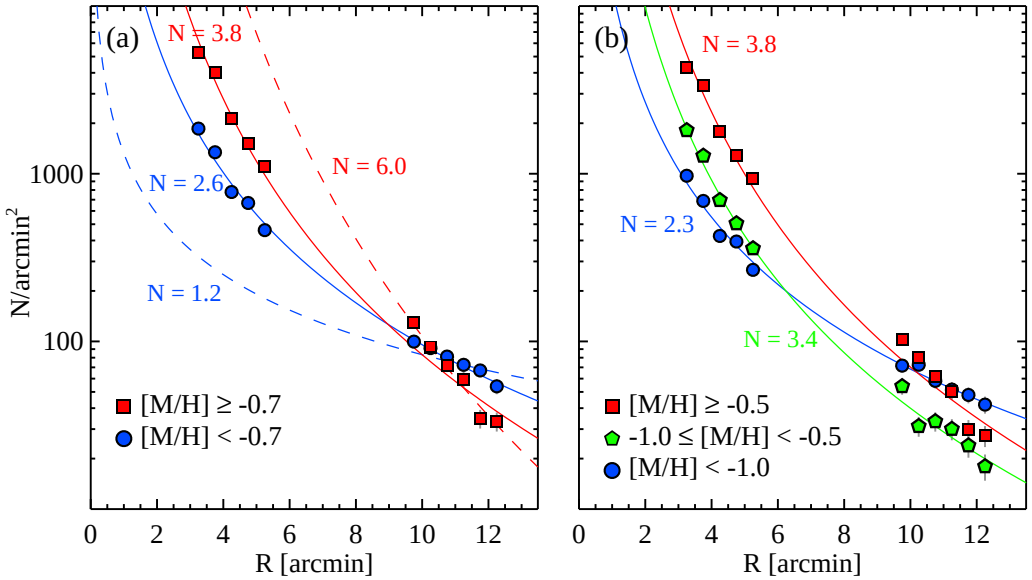

FIG. 9.— Same as **Figure 8**, but for the power law fits. Dashed lines represent the power law fit results that Harris et al. (2007b) derived for the outer region ($9' < R < 13'$) only: $N = 1.2 \pm 0.7$ for the metal-poor stars and $N = 6.0 \pm 0.6$ for the metal-rich stars. Note that they do not match the data for the inner region.

outer region. Thus the contribution of the low metallicity tail of the metal-rich component to this range is 6.8% in the inner region and 8.6% in the outer region. Thus there may be some selection bias in the derived radial profiles with a given [M/H] cut value. To check this, we divided the [M/H] range into three groups [M/H] < -1, (–1 to –0.5), and > -0.5, and derived the radial profiles for each, as shown in the right panels of **Figures 8** and **9**. In this case, the range [M/H] < -1.0 covers 55% of the metal-poor component in the inner region, and 76% in the outer region. The contribution of the low metallicity tail of the metal-rich component to this range is 3.0% in the inner region and 3.5% in the outer region. It is expected that the radial profiles of the metal-poor component for [M/H] $= -1.0$ cut will be flatter than that for [M/H] $= -0.7$ cut. This is seen in **Figures 8(b)** and **9(b)**: the power index of the metal-poor component for [M/H] $= -0.7$ cut is $N = 2.58 \pm 0.03$, which is slightly larger than the value for [M/H] $= -1.0$ cut, $N = 2.28 \pm 0.02$. On the other hand, the value of the power law index for the metal-rich component does not change depending on the [M/H] cut value, with $N = 3.83 \pm 0.03$ for [M/H] ≥ -0.7 and $N = 3.82 \pm 0.02$ for [M/H] ≥ -0.5. Thus there is some selection bias in the radial profiles due to

the [M/H] cut value, but it is not significant.

4. DISCUSSION

4.1. *Analytic Chemical Evolution Models for the MDFs*

Simple analytic chemical evolution models have been used to investigate how galaxies evolve from the comparison with the MDFs of resolved stars in nearby galaxies (Talbot & Arnett (1971); Lynden-Bell (1975); Tinsley (1980); Pagel (1997); Harris et al. (2007a,b); Kirby et al. (2011); Peacock et al. (2015) and references therein). We compared the MDFs of the resolved stars in M105 with three analytic chemical evolution models, as applied to the studies of the Local Group dwarf spheroidal galaxies by Kirby et al. (2011) and NGC 3115 by Peacock et al. (2015): a pristine closed-box model, a pre-enriched closed-box model, and an accreting gas model.

First, the pristine closed-box model is based on the assumptions that a galaxy is a closed-box with no inflow or outflow, that gas is converted only by star formation, and that initial gas (pristine gas) is metal-free. This model predicts an MDF:

$$N([\mathrm{M/H}]) \propto (10^{[\mathrm{M/H}]}) \exp(\frac{-10^{[\mathrm{M/H}]}}{p}),$$

where p is a metal yield that is a ratio of the mass of metals newly produced by the new generation of stars and the total mass in the survived stars among them. The higher the value of p is, the higher the value of the peak metallicity in the MDF is.

Second, the pre-enriched closed-box model allows initial gas to be enriched with $[\mathrm{M/H}]_0$, to reduce the well-known G-dwarf problem. This model predicts an MDF:

$$N([\mathrm{M/H}]) \propto (10^{[\mathrm{M/H}]} - 10^{[\mathrm{M/H}]_0}) \exp(\frac{-10^{[\mathrm{M/H}]}}{p}).$$

Third, the accreting gas model (the extra gas model or the best accretion model (Lynden-Bell 1975; Pagel 1997; Kirby et al. 2011)) allows external gas to accrete to the galaxy during its evolution. In this model we can describe the relation between the fraction of the gas mass with respect to the initial gas mass g and that of the stellar mass s by $g(s) = (1 - s/M)(1 + s - s/M)$ where M is the final stellar mass in units of the initial gas mass. M can be larger than one in this model, while $M = 1$ in the closed-box models. In this model the free parameters are p and M. This model predicts an MDF that is much narrower than the closed-box models, as described by

$$N([\mathrm{M/H}]) \propto \frac{10^{[\mathrm{M/H}]}}{p} \frac{1 + s(1 - 1/M)}{(1 - s/M)^{-1} - 2(1 - 1/M)(10^{[\mathrm{M/H}]}/p)}.$$

Here the relation between s and [M/H] is not simple, but is given in a complicated form by

$$[\mathrm{M/H}](s) = \log(p(\frac{M}{1 + s - s/M})^2 \ln(\frac{1}{1 - s/M} - \frac{s}{M}(1 - \frac{1}{M})).$$

We fit the MDFs of the bright RGB stars with $M_{\mathrm{bol}} \leq -3.0$ mag in M105 using these models, summarizing the results in **Table 5** and **Figure 10**. We tried to find the best-fit values of the parameters using least-squares minimization in the parameter space. For model fitting we used the MDFs for the range [M/H]≤ 0.3 where incompleteness is not serious. In the case of the accreting gas models, we tried both single component models and double component models (metal-rich one and metal-poor one), finding that the latter fit better the MDFs than the former. Errors for the parameters were calculated using the bootstrapping method with 1000 trials. In the double component modeling, we fit first the metal-rich part of the MDFs ($-0.6 <$[M/H]≤ 0.3) using an accreting gas model as shown by the solid lines, and subtract the resulting model from the MDF. Then the residual MDF is fit using another model. Then we subtract this model from the original MDF, and fit the it with an accreting gas model. We iterate this procedure until the entire MDF is fit well by the double component models.

Figure 10 shows several interesting features. First, in the case of single component models (top panels), the MDF of the inner region is fit reasonably well by the accreting gas model, but not by any of the closed-box models. On the other hand, the MDF of the outer region is poorly fit with any of the models. The MDF of the outer region shows a significant excess above the accretion model in the low metallicity range, while that of the inner region reveals a weak excess in the similar low metallicity range at [M/H]≤ -0.7.

Second, the MDFs of both regions are fit remarkably well by the accreting gas model with double components (middle panels). To show better the MDFs of the metal-poor component only, we subtracted the metal-rich component models from the original MDF, and displayed the residuals in the bottom panels. The errorbars in the residual MDFs represent Poisson errors of the original MDFs. It has been generally assumed in the chemical evolution models that the yield (p) does not vary depending on metallicity. If the yield is a function of metallicity, a single-component accreting gas model would fit the data even for the low metallicity range. However, there are no physical justifications for this and nothing is known about how it varies as a function of metallicity.

Third, interestingly the residual MDFs show clearly an excess in the low metallicity range at [M/H]≤ -0.5 in both the inner and outer regions. The excess in the narrow high metallicity range at [M/H]> 0.0 for the inner region is dominated by the errors, as shown by the errorbars, and also by the larger uncertainty in the metallicity estimation so that it can be ignored. We fit the residual MDFs for [M/H]≤ -0.5 with single component models, finding that all three models fit reasonably well the residual MDFs. It is noted also that the shapes of the residual MDFs in both regions appear to be similar to those for the bright dwarf spheroidal galaxies (Kirby et al. 2011).

Fourth, in the accreting gas models with double components, the metal yield parameter for the metal-rich component ($p = (1.14 \pm 0.02)Z_{\odot}$) in the inner region is about one order of magnitude larger than that for the metal-poor component ($p = (0.10 \pm 0.02)Z_{\odot}$), while the final mass parameter for the metal-rich component ($M = 2.93 \pm 0.18$) for the inner region is about twice larger than that for the metal-poor component ($M = 1.35 \pm 0.63$). Similar trends are also seen in the outer region: $p = (0.90 \pm 0.04)Z_{\odot}$ and $M = 2.84 \pm 0.51$ for

TABLE 5
A Summary of Chemical Evolution Model Fits

Region	Component	Pristine closed-box $p(Z_\odot)$	Pre-enriched closed-box $p(Z_\odot)$	Pre-enriched closed-box $[M/H]_0$	Accreting gas $p(Z_\odot)$	Accreting gas M
Inner region	Single	0.84 ± 0.01	0.81 ± 0.01	-2.18 ± 0.03	1.14 ± 0.02	2.93 ± 0.18
Outer region	Single	0.62 ± 0.03	0.62 ± 0.03	≤ -4.0	0.79 ± 0.02	1.36 ± 0.51
	Double					
Inner region	Metal-rich				1.14 ± 0.02	2.93 ± 0.18
	Metal-poor	0.11 ± 0.01	0.10 ± 0.01	-2.42 ± 0.03	0.10 ± 0.02	1.35 ± 0.63
Outer region	Metal-rich				0.90 ± 0.04	2.84 ± 0.51
	Metal-poor	0.06 ± 0.01	0.05 ± 0.01	-2.29 ± 0.01	0.06 ± 0.01	1.83 ± 0.56

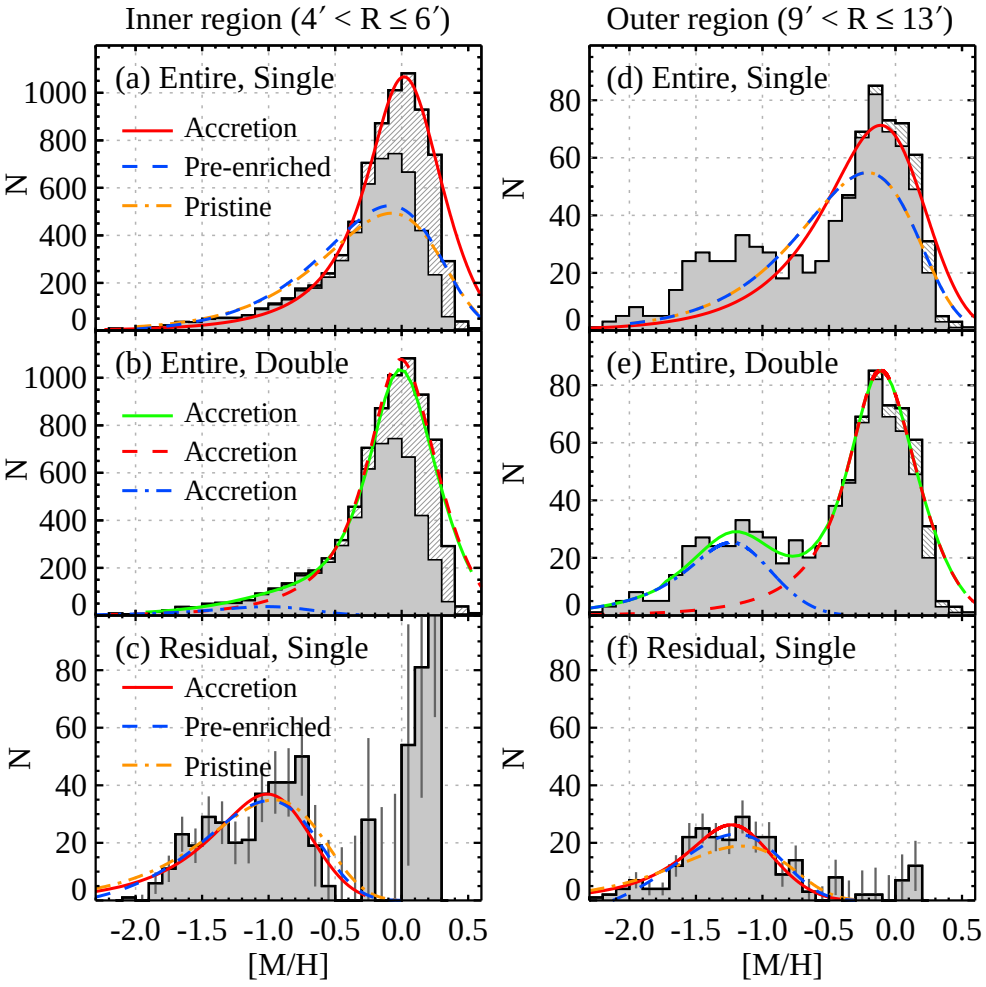

Fig. 10.— Chemical evolution models for the MDFs of the bright RGB stars ($M_{\rm bol} \leq 3.0$) in the inner region ($4' < R \leq 6'$) (left panels) and outer region ($9' < R \leq 13'$) (right panels) of M105. (Top panels) Single component models. (Middle panels) Double component accreting gas models. The fitting range for the chemical evolution models is [M/H]< +0.3. (Bottom panels) The residual MDFs after subtraction of the metal-rich component in the accreting gas model. Yellow dot-dashed lines, blue dashed lines, and red solid lines denote the pristine closed-box models, the pre-enriched closed-box models, and the accreting gas models, respectively. Fitting parameters for the models are listed in **Table 5**.

the metal-rich component, and $p = (0.06 \pm 0.01)Z_\odot$ and $M = 1.83 \pm 0.56$ for the metal-poor component.

Fifth, the size ratio of the metal-rich component and the metal-poor component is 21.6:1.0 for the inner region, and 2.4:1.0 for the outer region. Thus the contribution of the metal-poor component is minor (4.4%) in the inner region, but it becomes significant (29.4%) in the outer region.

Sixth, in the accreting gas models with double components, the peak metallicity of the metal-rich component in the inner region ([M/H]$\approx$ 0.0) is only 0.1 dex higher than that for the outer region ([M/H]≈ -0.1). Interestingly the peak metallicity of the metal-poor component in the inner region ([M/H]≈ -1.0) is about 0.2 dex higher than that for the outer region ([M/H]≈ -1.2). Thus the metallicity gradient of each component be-

TABLE 6
A Summary of HST Data for Nearby Early-type Galaxies

Parameter	Virgo Core Field	NGC 5128	NGC 3377	NGC 404	NGC 5011C	ESO410-005
P.I.	10131	9373	9811	10915	12546	10503
R.A.(2000)	12 28 10.9	13 25 14.01	10 47 48.1	01 09 17.0	13 13 11.9	00 15 32.2
Dec(2000)	+12 33 21	–43 34 27.8	+13 55 45	+35 44 46	–43 15 56	–32 10 36
Instrument	ACS/WFC	ACS/WFC	ACS/WFC	WFPC2	ACS/WFC	ACS/WFC
T(exp), F606W	63,440s	30,880s	38,500s	36,400s	900s	13,440s
T(exp), F814W	26,880s	30,880s	22,260s	36,400s	900s	26,880s

TABLE 7
A Summary of Basic Information for Nearby Early-type Galaxies

Parameter	M105	Virgo Core Field[a]	NGC 5128	NGC 3377	NGC 404	NGC 5011C	ESO410-005	Reference
R.A.(2000)	10 47 49.6	12 30 49.4 (M87)	13 25 27.6	10 47 42.3	01 09 27.0	13 13 11.9	00 15 31.5	1
Dec(2000)	+12 34 54	+12 23 28 (M87)	–43 01 09	+13 59 09	+35 43 05	–43 15 56	–32 10 48	1
Type	E1	cD pec (M87)	Ep	E5-6	SA0	S0pec	dE3	1,2
B	10.24	9.59	7.78	11.24	11.21	14.37	14.93	2,3
$B-V$	0.96	0.96	1.00	0.86	0.94	0.9[b]	0.9[b]	2,3
V	9.28	8.63	6.78	10.38	10.27	13.47[b]	14.03[b]	2,3
I		7.92				13.25	13.86	3
$E(B-V)$	0.022	0.020	0.101	0.030	0.051	0.106	0.012	1,4
$E(V-I)$	0.030	0.028	0.142	0.042	0.072	0.150	0.017	1,4
A_V	0.069	0.063	0.315	0.093	0.160	0.331	0.037	1,4
A_I	0.037	0.035	0.173	0.051	0.088	0.181	0.020	1,4
			Distance estimation					
I_{TRGB}	26.02 ± 0.02	26.97 ± 0.03	23.91 ± 0.03	26.19 ± 0.02	23.50 ± 0.02	24.00 ± 0.02	22.37 ± 0.02	5
A_I	0.039	0.038	0.185	0.050	0.078	0.181	0.020	1,4
$I_{0,TRGB}$	25.98 ± 0.02	26.93 ± 0.03	23.75 ± 0.03	26.14 ± 0.02	23.42 ± 0.02	23.82 ± 0.02	22.35 ± 0.02	5
$E(V-I)$	0.032	0.031	0.152	0.041	0.063	0.150	0.017	1,4
$(V-I)_{TRGB}$	1.58 ± 0.03	1.47 ± 0.02	1.88 ± 0.3	1.71 ± 0.03	1.66 ± 0.02	1.71 ± 0.02	1.43 ± 0.02	5
$M_{I,TRGB}$	–4.06	–4.09	–4.02	–4.04	–4.04	–4.06	-4.09	5
$(m-M)_0$	30.04 ± 0.02	31.02 ± 0.03	27.75 ± 0.03	30.18 ± 0.02	27.46 ± 0.02	27.88 ± 0.02	26.44 ± 0.02	5
M_V	–20.83	–22.45	–21.29	–19.89	–17.35	–14.74	–12.45	5

References. — (1) NED; (2) RC3 (de Vaucouleurs 1991); (3) Hyperleda; (4) Schlafly & Finkbeiner (2011); (5) This study.

[a] The Virgo core field is located at about $40'$ ($\sim$30 $R_{\rm eff}$) from the center of M87 (see **Figure 1** in Jang & Lee (2014)). We list the parameters for M87 derived in this study.

[b] Assumed.

tween the two regions (mean galactocentric distances of the stars in each component are $R = 11\farcm1$ and $4\farcm5$) is weak: d[M/H]/dLog(R) = −0.26 for the metal-rich component, and d[M/H]/dLog(R) = −0.51 for the metal-poor component. In contrast, the mean value of the metallicity of the entire bright RGB stars in the MDFs is [M/H] = -0.176 ± 0.005 for the inner region and [M/H] = -0.516 ± 0.021 for the outer region (median values are −0.050 and −0.350, respectively). Thus the metallicity difference between the two regions is Δ[M/H]= -0.34 ± 0.02, yielding a radial gradient of d[M/H]/dLog(R) = -0.87 ± 0.05. This value is a few times larger than the value for each of the metal-rich and metal-poor component. Therefore the metallicity gradient of the whole RGB in M105 is mainly a population gradient, not by a gradual change of the peak metallicity of single populations.

4.2. *Comparison of the MDFs of the ETGs*

Harris et al. (2007a) presented a comparison of the MDFs for RGB stars from dwarf galaxies (Draco, Leo I, NGC 147) to bright ETGs (NGC 3377, M105 and NGC 5128). They found that faint ETGs show only low metallicity stars, while the bright ETGs show low metallicity stars with an extremely broad range of metallicity as well as high metallicity stars, and that mean metallicity is higher for brighter (more massive) ETGs. Mould & Spitler (2010) found that the MDF of the RGB stars in the halo field of a very bright Sa galaxy, M104 (NGC 4594, Sombrero), is similar to those for the ETGs with similar luminosity, indicating that the chemical evolution of the halo in the disk galaxies may be similar to that of the ETGs.

We selected four ETGs with a wide range of luminosity to compare with M105: NGC 3377 (E5, $M_V = -19.89$), NGC 404 (dS0, $M_V = -17.35$), NGC 5011C (dS0, $M_V = -14.74$), and ESO410-005 (dE3, $M_V = -12.45$). Resolved stars in these galaxies were studied previously: NGC 3377 (Harris et al. 2007b), NGC 404 (Williams et al. 2010), NGC 5011C (Saviane & Jerjen 2007), and ESO410-005 (Da Costa et al. 2010; Tikhonov 2013; Yang et al. 2014). We also included one halo field at $R \approx 33'$ of NGC 5128 previously studied by Rejkuba et al. (2005). NGC 5128 (Ep, $M_V = -21.29$) is 0.5 mag brighter than M105.

In addition, we selected a field close to the Virgo center where there are no bright galaxies (called the Virgo core field). This field is located at about $40'$ ($\sim$30 $R_{\rm eff}$) from the center of M87 (see **Figure 1** in Jang & Lee (2014)).

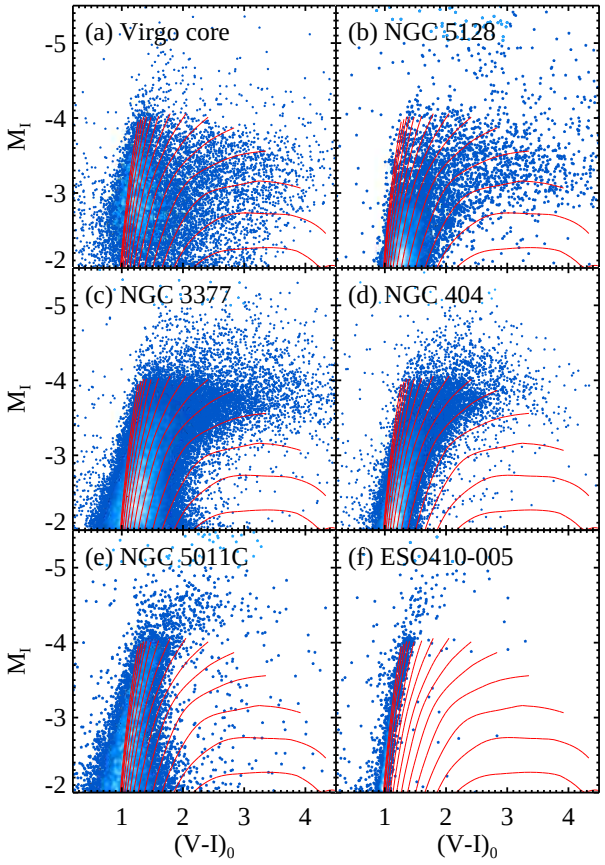

FIG. 11.— $M_I - (V-I)_0$ CMDs of the resolved stars in the Virgo Core Field, NGC 5218 (Ep, $M_V = -21.29$), NGC 3377 (E5, $M_V = -19.89$), NGC 404 (S0, $M_V = -17.35$), NGC 5011C (S0, $M_V = -14.74$), and ESO410-005 (dE3, $M_V = -12.45$). Red solid lines represent 12 Gyr isochrones for [α/Fe]=+0.2 and a range of metallicity ([M/H] = –2.2 to +0.4) with a step of 0.2 from left to right in the Dartmouth models (Dotter et al. 2008).

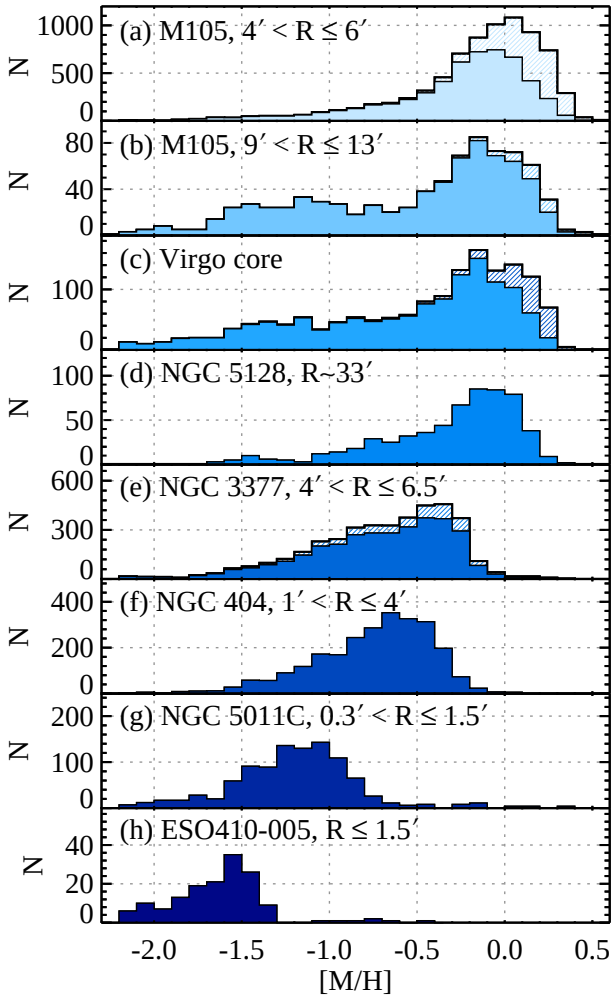

FIG. 12.— A comparison of MDFs of the resolved RGB stars in M105, the Virgo Core Field, NGC 5128 (Ep, $M_V = -21.29$), NGC 3377 (E5, $M_V = -19.89$), NGC 404 (S0, $M_V = -17.35$), NGC 5011C (S0, $M_V = -14.74$), and ESO410-005 (dE3, $M_V = -12.45$). The filled and hatched histograms represent the MDFs before and after completeness correction, respectively. Completeness corrections for other MDFs are negligible, as shown by their CMDs.

This field is far from nearby bright galaxies (including M87, M86 and M84), representing an intracluster field close to the Virgo center. Williams et al. (2007) presented a study of the intracluster stars in this field based on the HST F606W and F814W imaging. They suggested in the study of resolved stars in the Virgo core field that the population younger than 10 Gyr is more metal-rich than that older than 10 Gyr. They used Starfish CMD model fitting (Harris & Zaritsky 2001) and the isochrones given by Girardi et al. (2002) to derive the star formation history in this field. They found that this field is dominated by low metallicity old stars, but includes a small fraction of younger popoulation with high metallicity. Thus the MDF of this field we derived with 12 Gyr isochrones may be affected by the presence of younger population in this field, but the effect may be minor.

A summary of HST data and basic properties of these galaxies are listed in **Table 6** and **7**. We obtained photometry of the resolved stars in each galaxy from the F606W and F814W images in the HST archive, using the same procedures as done for M105. We determined the distances to these galaxies using the TRGB method.

Figure 11 displays the CMDs of the resolved stars in these galaxies and the Virgo core field . Absolute magnitudes and intrinsic colors of the resolved stars were derived, adopting the distances derived in this study and foreground reddening values (Schlafly & Finkbeiner 2011) for each galaxy. We also overlayed 12 Gyr isochrones for [α/Fe] = 0.2 and a range of metallicity ([M/H] = –2.2 to 0.4) (Dotter et al. 2008). Then we derived the metallicity of the resolved stars using the same procedures as done for M105. In **Figure 11** all galaxies show prominent RGBs. However, the width of the RGB gets narrower and the mean color of the RGB gets bluer, as their host galaxies become fainter.

In **Figure 12** we compare the MDFs for the bright RGB stars in the inner and outer regions of M105 ($4' < R \leq 6'$ and $9' < R \leq 13'$) and those in other galaxies and the Virgo core field. Several distinguishable features are found in this figure. First, the MDF of the outer region in M105 is remarkably similar to that of the intracluster field in the Virgo. Both MDFs show two major components and their peak positions are similar ([M/H] ≈ -1.2 and –0.1, respectively). This shows that the outer field of massive galaxies and intracluster field close to the center of galaxy clusters may share a similar history of grow-

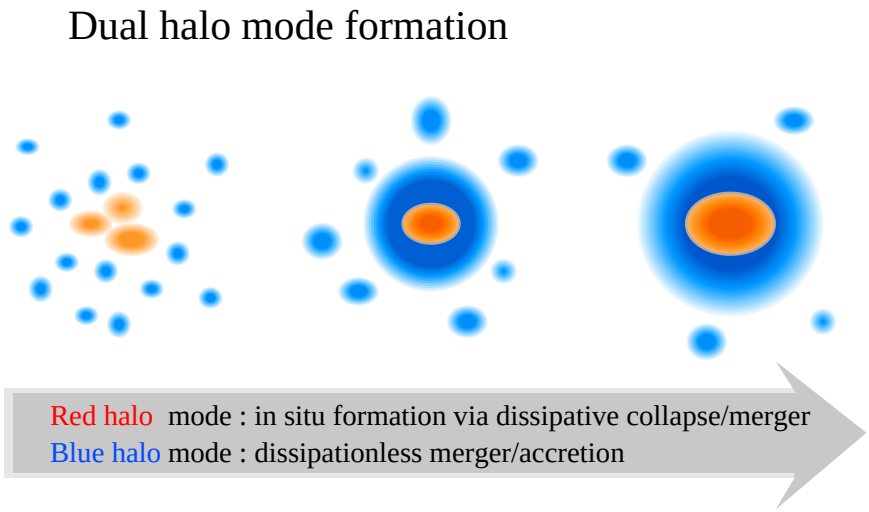
Dual halo mode formation
Red halo mode : in situ formation via dissipative collapse/merger
Blue halo mode : dissipationless merger/accretion

FIG. 13.— A schematic sketch for the dual halo mode formation scenario to explain how massive ETGs are formed. In the first phase of the red halo mode, red halos dominated by metal-rich stars are formed in the massive progenitors (either a single massive protogalactic cloud or merger of two or more massive galaxies), while blue halos of metal-poor stars are formed in the low-mass galaxies around the massive progenitors more than 10 Gyrs ago. In the second phase of the red halo mode, red halos grow via merger of intermediate-to-high mass galaxies, becoming larger and more massive. In the blue halo mode, the blue halos around the massive red halos grow via dry mergers of low-mass galaxies for long until today.

ing. The existence of the significant metal-rich component with [M/H] ≈ -0.1 in both the outer halo of M105 and the Virgo core field implies that a significant fraction of the progenitors for the stars in these low density regions are massive galaxies (as massive as M105). Second, the peak metallicity of the high metallicity component in each galaxy is higher for brighter galaxies, consistent with the results in Harris et al. (2007a). Third, the peak metallicity of the metal-poor component in M105 (as well as in the Virgo core field) is similar to that of NGC 5011C ($M_V = -14.7$ mag). This implies that the progenitors of these metal-poor components are probably dwarf galaxies with $M_V = -14$ to –15 mag. Fourth, the progenitors of the metal-poor stars at the very low metallicity tail ([M/H]< -1.5) in M105 are, in part, fainter dwarf galaxies with $M_V > -12.0$ mag (dSphs and UFDs). Some of them may have come from the early stages of star formation in the central galaxy.

4.3. *Dual Stellar Halos and Formation of Massive ETGs*

Key results found in this study are 1) that the MDF of the bright RGB stars in the large range of galactocentric distance of M105 is bimodal, 2) that the metal-poor component is getting more dominant in the outer region of a galaxy, 3) that the radial number density profiles of the metal-rich and metal-poor stars in M105 are significantly different in the outer region, 4) that the radial number density profiles of the metal-rich and metal-poor stars in M105 are fitted well by the Sersic law with $n \approx 2.8$ and $n \approx 6.9$, respectively, 5) that the peak metallicity of the metal-rich component in the outer halo of M105 is similar to that of the Virgo core field, 6) that the peak metallicity of the metal-poor component in M105 (as well as in the Virgo core field) is similar to that of NGC 5011C ($M_V = -14.7$ mag), and 7) that the progenitors of the metal-poor stars at the low metallicity tail ([M/H] < -1.5) in M105 are possibly fainter dwarf galaxies with $M_V > -12.0$ mag (dSphs and UFDs).

These results indicate that there are two distinct stellar halos in massive ETGs like M105: a metal-poor (blue) halo and a metal-rich (red) halo. The metal-rich halo is dominant in the inner region, while the metal-poor halo is more distinguishable in the outer region. Harris et al. (2007b) found the existence of a distinguishable blue RGB in the study of the same outer field as used in this study, and predicted that "large E/S0 galaxies in general will have diffuse, very low-metallicity halo components, but that photometry at radii ($R \sim (10-15)R_{\rm eff}$) will be necessary to find them". Since then these diffuse low-metallicity halo components have been found in the outer regions of a few E/S0 galaxies.

The existence of dual stellar halos in massive ETGs is consistent with the prediction based on the globular cluster systems in ETGs (Park & Lee 2013): massive ETGs may have often dual halos, one blue (metal-poor) halo and one red (metal-rich) halo. Considering the properties of red and blue globular cluster systems in massive ETGs, Park & Lee (2013) suggested a dual halo scenario for how massive ETGs formed. Massive ETGs are formed in two main modes: a metal-rich halo mode and a metal-poor halo mode.

We provide an updated scenario, including the information we found from the stellar halos in this study. **Figure 13** illustrates a schematic view of the main features of this scenario. This scenario is based on the concept of hierarchical merging models for structure formation (Côté et al. (1998); De Lucia & Blaizot (2007); Contini et al. (2014); Cooper et al. (2015); Hirschmann et al. (2015); Somerville & Davé (2015) and references therein), focusing on the observational results on the properties of the resolved stars and globular clusters in ETGs. All galaxies should have different formation histories, because they start with progenitors with different masses and are involved with diverse histories of merging. However, considering the bimodality of the MDFs of the resolved stars in ETGs, we can divide the formation modes roughly into two: a metal-rich halo

mode and a metal-poor mode.

In the metal-rich halo mode, metal-rich halos formed in two phases. In the first phase, during the early phase of the universe, progenitors of today's massive galaxies formed via rapid collapse of massive protogalactic clouds (in situ formation of stars) (Eggen et al. 1962) and/or major mergers, while a much larger number of low mass galaxies and globular clusters formed via collapse of low mass clouds embedded in low mass dark matter halos mostly around the massive galaxies (Searle & Zinn 1978; White & Rees 1978). These two processes (in situ collapse and major mergers) in the massive progenitors are not independent, but both can happen in the same galaxy with a small time lag. Major mergers can be either wet or dry and they can be involved also with several mergers. In this mode, the MDF of the stars in the massive galaxies will show a dominant metal-rich component with a weak tail in the low metallicity end, as described in classical chemical evolution models. The larger the masses of the most massive progenitors are, the higher the peak values of the stellar metallicity are. The structure, color, and luminosity of the resulting galaxies are dominated by the metal-rich stars. In the second phase, the metal-rich halos grow mostly via merging with intermediate mass galaxies that have metallicities higher than those of dwarf galaxies. The MDFs in the resulting galaxies will be broader toward the low metallicity. They will be involved with numerous merging with low-mass/dwarf galaxies as well, but it will contribute only a minor role in increasing the mass and size of the metal-rich halos. Thus the metal-rich halos formed and evolve in two phases, being dominated by metal-rich stars.

In the metal-poor halo mode, metal-poor halos grow mainly via accretion or minor mergers of dwarf galaxies for long duration. The outstanding existence of a distinct blue (metal-poor) RGB in the outer region of massive galaxies shows that they are not the low metallicity tail of the main population (the metal-rich halo), but they have a distinct origin. The origin of the metal-poor stars is considered to be accreted dwarf galaxies that have mainly low metallicity stars with [M/H]< -1.0. Some brighter dwarf galaxies like NGC 5011C ($M_V \sim -15.0$ mag) produce the metal-poor component peak at [M/H]~ -1.2. Among the dwarf galaxies, ultra-faint dwarf galaxies (UFDs) are one of the strong candidates for the low metallicity tail at [M/H]< -1.5. UFDs have been found mostly in the Local Group (Belokurov 2013). The stellar populations in several nearby UFDs in the Local Group (Brown et al. 2014) and the Virgo cluster (Jang & Lee 2014) are known to be old and metal-poor, consistent with the halo stars in the low metallicity tail in M105. These dwarfs are accreted in the outer region of a galaxy, contributing to the growth of the metal-poor halo. Thus the accreted stars in the metal-poor halo must be very old, although they join the metal-poor halo during the long period. The number density of the metal-poor stars is very low so that they make only a minor contribution to the luminosity of the galaxies. However, they contain critical clues to understand how and when the outer halo formed and to study the distribution of the dark matter.

This dual halo mode scenario, mainly based on observational results of resolved red giants and globular clusters in nearby galaxies, is consistent with the two-phase scenario derived from high-resolution cosmological simulations (Oser et al. (2010, 2012); Hirschmann et al. (2015) and references therein). In the first phase of this scenario, compact cores of massive galaxies form rapidly via in-situ star formation associated with cold flows and/or gaseous mergers early at $2 < z < 6$. These compact massive galaxies will have, on average, $M \approx 10^{11} M_{\odot}$, $R_{\rm eff} \approx 1$ kpc, and $\sigma_v \approx 240$ km s^{-1}, around the end of this phase, and they will show disk-like structures flatter than today's ETGs. Then in the second phase, these compact massive galaxies get bigger mainly via minor dry merging. The effective radii of these galaxies grow significantly faster in size than in mass as a result of conservation of angular momentum, and they will have lower velocity dispersion in the central region. As time goes on, these galaxies will have larger outer envelopes, which also grow in mass, occupying a major fraction of mass in more massive galaxies. However, note that there are other views in the literature. For example, noting the abundance of compact massive bulges in nearby disk galaxies, Graham et al. (2015) concluded that not all compact massive galaxies at high redshift grow dramatically in size. Instead some of them keep their compactness, being embedded in disks that grow slowly for long. This scenario has been successful in explaining several observational results on the integrated properties of galaxies (Oser et al. 2012). The results on the resolved stars in M105 and other ETGs in this study provide another strong constraint to test the formation scenarios based on cosmological simulations. In particular the bimodal MDFs of the resolved stars in ETGs including these galaxies need to be considered in the future simulations.

5. SUMMARY AND CONCLUSION

Using deep photometry of the resolved stars in the large range of galactocentric distance ($3R_{\rm eff} \lesssim R \lesssim 13R_{\rm eff}$) of M105, a standard elliptical galaxy, we provided strong evidence that there are two subpopulations of RGB stars in this galaxy and investigated their structure and MDFs. We also presented the MDFs of the bright RGB stars in other nearby ETGs with a range of luminosity as well as in the Virgo core field derived using the same procedures as used for M105. Then we described the MDFs of M105 using the chemical evolution models, and discussed the implications of the results in terms of the dual halo mode formation scenario to explain how massive ETGs formed. Primary results are summarized as follows.

- The resolved stars in M105 are mostly RGB stars. We measured the TRGB magnitudes using an edge-detection method for the inner and outer region, obtaining $I_{\rm TRGB} = 26.02 \pm 0.02$. From the mean of the inner and outer regions, we obtain a distance modulus $(m-M)_0 = 30.05 \pm 0.02$(random)$\pm$ 0.12(systematic). This confirms that M105 is a member of the Leo I Group.

- The bright RGB stars in the CMDs and their color distributions show the existence of two distinct subpopulations: a strong red RGB with a broad color range and a weaker blue RGB with a narrower color range.

- We derived metallicities of the bright RGB stars from the comparison of their photometry with theoretical isochrones for 12 Gyr age. The MDF of the RGB stars in M105 also shows the existence of two distinct subpopulations: a dominant metal-rich population (with a peak at [M/H]$\sim$ 0.0) and a much weaker metal-poor population (with a peak at [M/H]~ -1.1).

- We divided the bright RGB stars into two groups according to their metallicity: a metal-poor one (-2.4 <[M/H]$\leq$ -0.7) and a metal-rich one (-0.7 <[M/H]$\leq +0.5$). The radial number density profile of the metal-rich RGB stars is significantly steeper than that of the metal-poor RGB stars in the outer region, while the slopes of both are similar in the inner region. The number density of the metal-rich stars is much higher than that of the metal-poor stars in the inner region at $R < 12'$, but becomes lower thereafter. The radial number density profiles of the metal-rich and metal-poor RGB stars in the entire range of galactocentric distance are fit well by a Sérsic law with $n = 2.75 \pm 0.10$ and $n = 6.89 \pm 0.94$, respectively. They are also fit by a single power law: $\sigma \propto R^{-3.83\pm0.03}$ for the metal-rich stars and $\sigma \propto R^{-2.58\pm0.03}$ for the metal-poor stars.

- The MDFs of both the inner region and the outer region can be described remarkably well by accreting gas models of chemical evolution with two components, a metal-rich one and a metal-poor one. The peak metallicity of the metal–rich component in the inner region is only 0.1 dex higher than that for the outer region. The metal-poor components also show a similar trend. The radial gradient of the metallicity between the two regions is dominated by the population mixture, rather than by the continuous change of the peak metallicity.

- These results provide strong evidence that there are two types of stellar halos in M105: a metal-poor (blue) and a metal-rich (red) halo. This is consistent with the prediction in the dual halo scenario based on the spatial distribution of the globular clusters in bright ETGs by Park & Lee (2013).

- Comparing the MDFs of the resolved stars in M105 with those of the resolved stars in faint to bright ETGs and in the intracluster field of the Virgo core, we suggested a dual halo mode scenario for the formation of massive ETGs.

The authors are thankful to anonymous referee for her/his useful comments which improved significantly our original manuscript. This work was supported by the National Research Foundation of Korea (NRF) grant funded by the Korea Government (MSIP) (No. 2012R1A4A1028713). This paper is based on image data obtained from the Multimission Archive at the Space Telescope Science Institute (MAST).

REFERENCES

Belokurov, V. 2013, NewAR, 57, 100
Bird, S. A., Flynn, C., Harris, W. E., & Valtonen, M. 2015, A&A, 575, 72
Bose, S., & Kumar, B. 2014, ApJ, 782, 98
Brodie, J. P., & Strader, J. 2006, ARA&A, 44, 193
Brown, T. M., Tumlinson, J., Geha, M., et al. 2014, ApJ, 796, 91
Busarello, G., Capaccioli, M., D'Onofrio, M., et al. 1996, A&A, 314, 32
Capaccioli, M., Held, E. V., Lorenz, H., & Vietri, M. 1990, AJ, 99, 1813
Cappellari, M., McDermid, R.M., Alatalo, K. et al. 2013, MNRAS, 432, 1862
Chaboyer, B., Green, R.G., & Liebert, J. 1999, AJ, 117, 1360
Ciardullo, R., Jacoby, G. H., & Tonry, J. L. 1993, ApJ, 419, 479
Ciardullo, R., Feldmeier, J. J., Jacoby, G. H., et al. 2002, ApJ, 577, 31
Contini, E., De Lucia, G., Villalobos, A., Borgani, S. 2014, MNRAS, 437, 3787
Cooper, A.P., Parry, O.H., Lowing, B. Cole, S., & Frenk, C. 2015, arXiv:1501.04630
Côté, P., Marzke, R.O., & West, M. J. 1998, ApJ, 501, 554
Crnojević, D., Ferguson, A. M. N., Irwin, M. J., et al. 2013, MNRAS, 432, 832
Da Costa, G.S., & Armandroff, T.E. 1990, AJ, 100, 162
Da Costa, G.S., Rejkuba, M., Jerjen, H., & Grebel, E.K. 2010, ApJ, 708, L121
De Lucia, G., & Blaizot, Jérémy 2007, MNRAS, 375, 2
de Vaucouleurs, G. 1975, Galaxies and the Universe, 557
de Vaucouleurs, G., & Capaccioli, M. 1979, ApJS, 40, 699
de Vaucouleurs, G., de Vaucouleurs, A., Corwin, H. G., Jr., et al. 1991, Third Reference Catalogue of Bright Galaxies (RC3) (New York: Springer)
Dotter, A., Chaboyer, B., Jevremović, D., et al. 2008, ApJS, 178, 89
Eggen, O. J., Lynden-Bell, D.;, & Sandage, A. R. 1962, ApJ, 136, 748
Elson, R. A. W. 1997, MNRAS, 286, 771
Garnavich, P.M., VandenBerg, D.A., Zurek, D.R., & Hesser, J.E. 1994, AJ, 107, 1097
Girardi, L., Bertelli, G., Bressan, A., Chiosi, C., Groenewegen, M. A. T., Marigo, P., Salasnich, B., & Weiss, A. 2002, A&A, 391, 195
Graham, A., Dullo, B.T., & Savorgnan, A.D. 2015, ApJ, 804, 32
Geisler, D., Lee, M. G., & Kim, E. 1996, AJ, 111, 1529
Gregg, M. D., Ferguson, H. C., Minniti, D., Tanvir, N., & Catchpole, R. 2004, AJ, 127, 1441
Harris, W. E. 1996, AJ, 112, 1487 (updated version in 2010, arXiv1012.3224)
Harris, G. L. H. & Harris, W. E. 2000, AJ, 120, 2423
Harris, J., & Zaritsky, D. 2001, ApJS, 136, 25
Harris, W. E., & Harris, G. L. H. 2002, AJ, 123, 3108
Harris, W. E., Harris, G. L. H., Layden, A. C., & Stetson, P. B. 2007, AJ, 134, 43
Harris, W. E., Harris, G. L. H., Layden, A. C., & Wehner, E. M. H. 2007, ApJ, 666, 903
Harris, G. L. H. 2010, PASA, 27, 475
Hirschemann, M., Naab, T., Ostriker, J.P. et al. 2015, MNRAS, 449, 528
Jang, I. S., & Lee, M. G. 2014, ApJ, 795, LL6
Jensen, J. B., Tonry, J. L., Barris, B. J., et al. 2003, ApJ, 583, 712
Jordán, A., Peng, E. W., Blakeslee, J. P., et al. 2009, ApJS, 180, 54
Karachentsev, I. D., & Karachentseva, V. E. 2004, Astronomy Reports, 48, 267
Kirby, E. N., Lanfranchi, G. A., Simon, J. D., Cohen, J. G., & Guhathakurta, P. 2011, ApJ, 727, 78
Larsen, S. S., Brodie, J. P., Huchra, J. P., Forbes, D. A., & Grillmair, C. J. 2001, AJ, 121, 2974
Lee, M. G., Freedman, W. L., & Madore, B. F. 1993, ApJ, 417, 553
Lee, M. G., & Jang, I. S. 2013, ApJ, 773, 13
Lynden-Bell, D. 1975, VA, 19, 299
Makarov, D., Prugniel, P., Terekhova, N., Courtios, H., & Vauglin, I. 2014, A&A, 570, 13
Méndez, B., Davis, M., Moustakas, J., et al. 2002, AJ, 124, 213
Mould, J., & Spitler, L. 2010, ApJ, 722, 721
Muratov, A. L., & Gnedin, O. Y. 2010, ApJ, 718, 1266
Oser, L., Ostriker, J.P., Naab, T., Johansson, P. H., & Burkert, A. 2010, ApJ, 725, 2312
Oser, L., Naab, T., Ostriker, J.P., & Johansson, P. H. 2012, ApJ, 744, 63
Pagel, B. E. J. 1997, Nucleosynthesis and Chemical Evolution of Galaxies (Cambridge: Cambridge Univ. Press)
Park, H. S., & Lee, M. G. 2013, ApJ, 773, LL27

Peacock, M. B., Strader, J., Romanowsky, A. J., & Brodie, J. P. 2015, ApJ, 800, 13
Peng, E. W., Jordán, A., Côté, P., et al. 2008, ApJ, 681, 197
Rejkuba, M., Greggio, L., Harris, W. E., Harris, G. L. H., & Peng, E. W. 2005, ApJ, 631, 262
Rejkuba, M., Harris, W. E., Greggio, L., & Harris, G. L. H. 2011, A&A, 526, AA123
Rejkuba, M., Harris, W. E., Greggio, L., et al. 2014, ApJ, 791, LL2
Rizzi, L., Tully, R. B., Makarov, D., et al. 2007, ApJ, 661, 815
Saviane, I. & Jerjen, H. 2007, AJ, 133, 1756
Sakai, S., Madore, B. F., & Freedman, W. L. 1996, ApJ, 461, 713 Makarov
Sakai, S., Madore, B. F., Freedman, W. L., et al. 1997, ApJ, 478, 49
Schlafly, E. F., & Finkbeiner, D. P. 2011, ApJ, 737, 103
Searle, L., & Zinn, R. 1978, ApJ, 225, 357
Sérsic, J. L. 1963, Boletin de la Asociacion Argentina de Astronomia La Plata Argentina, 6, 41
Sirianni, M., Jee, M. J., Benítez, N., et al. 2005, PASP, 117, 1049
Somerville, R., & Davé, R. 2015, ARA&A, in press (arXiv:1412.2712)
Stetson, P. B. 1994, PASP, 106, 250
Stierwalt, S.,Haynes, M.P., Giovanelli, R., Kent, B.R., Martin, A.M. et al. 2009, AJ, 138, 338 ,
Talbot, R. J., Jr., & Arnett, W. D. 1971, ApJ, 170, 409
Tikhonov, N. A. 2013, Astronomy Letters, 39, 298
Tinsley, B. M. 1980, Fundam. Cosm. Phys., 5, 287
Tonry, J. L., Dressler, A., Blakeslee, J. P., et al. 2001, ApJ, 546, 681
VandenBerg, D.A., Bergbusch, P.A., Dotter, A. et al. 2012, ApJ, 755, 15
VandenBerg, D.A., Bergbusch, P.A., & Edvardsson, B. 2014, ApJ, 794, 72
Watkins, A. E., Mihos, J. C., Harding, P., & Feldmeier, J. J. 2014, ApJ, 791, 38
Weijmans, A.-M., Cappellari, M., Bacon, R., et al. 2009, MNRAS, 398, 561
White, S. D. M.m, & Rees, M. J. 1978, MNRAS, 183, 341
Williams, B. F., Ciardullo, R., Durrell, P. R., et al. 2007, ApJ, 656, 756
Williams, B. F et al. 2010, ApJ, 716, 71
Yang, S.-C., Wagner-Kaiser, R., Sarajedini, A., Kim, S. C., Kyeong, J. 2014, ApJ, 784, 76